Regular Article

Probing cytoskeleton dynamics by intracellular particle transport analysis

M. Götz[1,2], K.F. Hodeck[1,2], P. Witzel[1,2], A. Nandi[3], B. Lindner[4,5], and D. Heinrich[1,6,a]

[1] Fraunhofer Institute for Silicate Research ISC, Neunerplatz 2, 97082 Würzburg, Germany
[2] Julius-Maximilians University Würzburg, Chemical Technology of Material Synthesis, Röntgenring 11, 97070 Würzburg, Germany
[3] Max-Planck-Institute for the Physics of Complex Systems, Nöthnitzer Straße 38, 01187 Dresden, Germany
[4] Humboldt University Berlin, Institute of Physics, Unter den Linden 6, 10099 Berlin, Germany
[5] Bernstein Center for Computational Neuroscience Berlin, Philippstr. 13, Haus 2, 10115 Berlin, Germany
[6] Leiden University, LION Leiden Institute of Physics, Niels Bohrweg 2, 2333 CA Leiden, The Netherlands

Abstract. All cellular functions arise from the transport of molecules through a heterogeneous, highly dynamic cell interior for intracellular signaling. Here, the impact of intracellular architecture and cytoskeleton dynamics on transport processes is revealed by high-resolution single particle tracking within living cells, in combination with time-resolved local mean squared displacement (I-MSD) analysis. We apply the I-MSD analysis to trajectories of 200 nm silica particles within living cells of *Dictyostelium discoideum* obtained by high resolution spinning disc confocal microscopy with a frame rate of 100 fps and imaging in one fixed focal plane. We investigate phases of motor-driven active transport and subdiffusion, normal diffusion, as well as superdiffusion with high spatial and temporal resolution. Active directed intracellular motion is attributed to microtubule associated molecular motor driven transport with average absolute velocities of $2.8\,\mu\mathrm{m\,s^{-1}}$ for 200 nm diameter particles. Diffusion processes of these particles within wild-type cells are found to exhibit diffusion constants ranging across two orders of magnitude from subdiffusive to superdiffusive behavior. This type of analysis might prove of ample importance for medical applications, like targeted drug treatment of cells by nano-sized carriers or innovative diagnostic assays.

[a] e-mail: doris.heinrich@isc.fraunhofer.de

1 Introduction

The general basis of all cellular functions are transport processes throughout the cell interior, such as the transport of proteins regulating signal transduction [1], gene transcription [2], reaction kinetics [3], and regulation of cell polarization [4]. As the interior of living cells represents a highly crowded and dynamic environment, transport processes are affected by collisional interactions with barriers consisting of organelles and large molecules, as well as active processes like molecular binding events and motor-driven transport [5–7]. Different models have been developed to theoretically describe this complex motion in media with disordered microscopic substructures [8–13].

Concerning the involved mechanisms, active, motor-assisted transport, and passive diffusion states are distinguished [14,15]. Basically, diffusive motion allows for a given species to effectively probe its local environment [16], whereas molecular motors, like kinesins or dyneins can carry a cargo in a fast and directed way over long distances, e.g. along microtubules [17,18]. For intracellular transport processes, these motility modes typically alternate on a sub-second time scale, at a rate that appears optimized for reaching a specific target within the cell as reliably and quickly as possible [19,20] or enhancing molecular reaction kinetics [21]. Various approaches on studying these dynamic intracellular processes have been established throughout the last years, e.g. tracking the motion of tracer particles [22,23], organelles [24] or molecules [22,25]. These approaches use different quantification strategies for motion parameters, like instantaneous velocities [26], step size [27], diffusion coefficient [28], and specifically for the mean squared displacement analysis [16,25,29].

The local mean squared displacement analysis

The mean squared displacement (MSD) $\langle r^2(t) \rangle$, giving the quadratic length of a particle's excursion, grows linear in time as $\langle r^2(t) \rangle \propto D \cdot t$ for Brownian motion in an isotropic medium, where D is the diffusion coefficient. Within a heterogeneous environment, like the interior of living cells, the MSD scales as $\langle r^2(t) \rangle \propto \tilde{D} \cdot t^\alpha$, with the non-dimensional MSD exponent α and a generalized diffusion coefficient $\tilde{D}$ characterizing anomalous diffusion [30]. Specifically, active ballistic motion (with a certain mean velocity in a given direction) is characterized by a MSD exponent $\alpha = 2$ [15], while diffusion is characterized by MSD exponents ranging from $0 < \alpha < 2$, reflecting the amount of deviation from normal diffusion corresponding to $\alpha = 1$ [31].

In general, the MSD analysis returns different results of α for anomalous transport in living cells, as the net result of the interplay of hindering and enhancing mechanisms [32,33]. Besides apparent subdiffusion with $\alpha < 1$ [34], on a macroscopic level also enhanced diffusion with MSD exponents $\alpha > 1$ is found [16,35], as well as transient α values between 0.75 and 1.5 [34]. Such differences partly arise from the fact that the MSD function reveals distinct transport states on different time scales. Short time scales are characteristically dominated by thermal diffusion [12], while the influence of active motion appears mostly on longer time scales [23]. In general, switching between intracellular motility states cannot be resolved by a standard global MSD analysis, hence information on the complex details of intracellular transport cannot be obtained. Therefore we introduced a local MSD (l-MSD) analysis algorithm providing an estimate of the MSD power law exponent and the diffusion coefficient as functions of time, this way allowing for a time-resolved trajectory analysis [23]. This approach is based on the local analysis of the MSD and directional persistence of motion, employing an adaptable lag time window sliding along the trajectory. The algorithm is capable of reliably separating different transport phases of a tracer by well-defined criteria [23].

The model organism Dictyostelium discoideum

Using this approach, we studied intracellular transport of tracer beads within living cells of *Dictyostelium discoideum* [22,23,31,36]. *D. discoideum* suits very well as a model organism, exhibiting a relatively simple cytoskeleton, which consists predominantly of a thin actin cortex close to the membrane, and a brush of microtubules (MT) connecting the cortex to the centrosome [37], while actin stress fibers and intermediate filaments are lacking [38]. Besides that, microscopic particles are readily endocytosed by *D. discoideum* cells and are enclosed in vesicles, ready for diffusion and motor driven transport [39]. Another method of internalization is ballistic injection [36]. In this case no vesicles are formed around the tracers and thus no active transport along MTs is possible.

Previous experimental investigations

The effect of motor protein activity for active transport along MTs was demonstrated by l-MSD analysis of the motion of $1.4\,\mu$m diameter Fe_3O_4 beads, endocytosed by wild-type cells [23]. Here, the l-MSD algorithm robustly distinguished active and passive transport states, revealing a sequence of equally spaced peaks in the active motion states. The corresponding velocities of $v_n = n \cdot v_1$, with $v_1 = 0.225\,\mu$m s^{-1} and $n = 1, 2, 3, 4$ suggest the coordinated activity of a finite number of molecular motors attached to different MTs [17,23,40–42]. In contrast, depolymerization of microtubules by Benomyl treatment of the cells led to the disappearance of active transport states. Analysis of passive motion corresponding to a median diffusion coefficient of $D^{\mathrm{med}} = 6.1 \times 10^{-3}\,\mu$m^2 s^{-1} [23] yielded a relatively low estimate [43,44] of the cytoplasm viscosity of $\eta_{\mathrm{c}} = 5 \times 10^{-2}$ Pa s [23], as in this study purely passive particle motion was probed. The possibility for temporal state analysis is introduced as another algorithm feature. The distribution of active state durations exhibits an exponential decrease with a characteristic time of $\tau_{\mathrm{act}} = 0.65$ s [23], whereas passive states show a more complex behavior characterized by a log-normal distribution of the state duration.

Further investigations focusing on how transport dynamics are influenced by cytoskeleton states were performed by tracking Fe_3O_4 particles of $1.0\,\mu$m diameter again internalized via endocytosis by *D. discoideum* cells exhibiting GFP labeled α-tubulin [22]. Selective removal of MTs led to a near-complete extinction of active motion states. Actin depolymerization by Latrunculin A caused a decrease in the overall number of active transport states, exhibiting lower active velocities of $\langle v_{\mathrm{act}}^{\mathrm{LatA}} \rangle = 0.58\,\mu$m s^{-1} [22], compared to $\langle v_{\mathrm{act}} \rangle = 0.62\,\mu$m s^{-1} [22] in untreated cells.

This shows that active MT associated transport is possible despite lacking anchorage of MTs to the outer actin cortex. This lack of anchorage yields in stronger MT coiling, causing non-straight transport trajectories with less detectable active states and apparently of lower speed values. The molecular motors, transporting the beads, move along bent MTs. These unanchored MTs move within the active, crowded cell interior. Moreover, increased D values are found suggesting a less densely packed cell interior in absence of the actin network and thus a more effective diffusion. The described measurements have also been performed exerting magnetic force on to the magnetic beads.

Intracellular transport dynamics were investigated further with ballistically injected polymer-coated γ-Fe_2O_3 beads of 150 nm diameter, in combination with simulation of a data driven model and lag time dependence analysis [36]. Here, diffusional states were selectively studied with a focus on α and D using the l-MSD algorithm for differentiation of passive motion states including subdiffusion and normal diffusion.

The removal of MTs led to a decrease of the diffusion constant from $\langle D^{\mathrm{WT}} \rangle = 6.10 \times 10^{-2} \, \mu\mathrm{m}^2 \, \mathrm{s}^{-1}$ [36] of wild type (WT) cells to $\langle D^{\mathrm{Beno}} \rangle = 3.53 \times 10^{-2} \, \mu\mathrm{m}^2 \, \mathrm{s}^{-1}$ [36], with lower α-values, caused by reduced intracellular dynamics due to the lack of MT sweeping motion and thus a more viscous cytoplasm. Actin depolymerization caused an increased diffusion constant of $\langle D^{\mathrm{LatA}} \rangle = 10.7 \times 10^{-2} \, \mu\mathrm{m}^2 \, \mathrm{s}^{-1}$ [36], and a small drop in α. In the absence of both, MT and F-actin, intracellular diffusion resembled Brownian-like motion with $\langle \alpha \rangle \approx 1$ and low diffusion coefficients (less than $1.1 \times 10^{-2} \, \mu\mathrm{m}^2 \, \mathrm{s}^{-1}$), indicating a major influence of dynamic cytoskeleton components on the cause of subdiffusion [36]. However, this only applies for lag times larger than $1.0 \, \mathrm{s}$, while at shorter lag times subdiffusion is still found, due to cytoplasmic crowding [36]. On basis of these results it is hypothesized that in healthy cells, MT sweeping yields a fluidization of the cytoplasm, facilitating particle diffusion on timescales ranging from $50 \, \mathrm{ms}$ to $2.5 \, \mathrm{s}$. The presence of filamentous actin is considered as a cause of short-range subdiffusion due to caging effects, in addition to intracellular crowding [36]. In addition, results from Refs. [22,36] suggest a strong influence of particle size on the transport mechanisms. The diffusion constant remains unchanged upon MT removal for $1.0 \, \mu\mathrm{m}$ diameter particles [22]. However, it declines by 42% for the 150 nm diameter particles [36]. These results relate to the complex cell interior built up on different length scales. The actin network and MTs match length scales of smaller particles, accounting for a strong influence on their motional behavior. Bigger particles experience hindrance on length scales of larger cell organelles, e.g. the endoplasmic reticulum and the golgi apparatus, or by the spatial limitations of the cell interior ($1.0 \, \mu\mathrm{m}$ diameter bead means 1/5 of the average cell diameter). These obstacles on the large scale cannot be removed without causing cell death. Therefore, our findings indicate an impact of the depolymerized cytoskeleton parts, like the MTs and the actin cortex, on the small investigated particle size.

Methodological considerations

In order to disentangle the influences of the analysis from the cellular properties on the statistical distributions of parameters obtained from the l-MSD, the parameter statistics of well-defined model systems were studied theoretically [45].

The analysis in [36] revealed that the subdiffusive phases of tracer motion can be reproduced with a simple model of Gaussian increments. In a temporally discretized version (suitable for comparison with experimental data), the dynamics in two spatial dimensions is given by [36]

$$x_i = x_{i-1} + v_i^x \Delta \mathrm{t}, \qquad y_i = y_{i-1} + v_i^y \Delta t \qquad (1)$$

with velocities $v_i^{x,y}$ that are Gaussian distributed variables. The stationary correlation functions of the $v_i^{x,y}$ can be extracted from the experimental increment statistics and can be numerically implemented by an autoregressive (AR) process [46]. Focusing on the latter, the velocity autocorrelation functions resemble the following function [45]

$$\langle v_i^x v_{i+k}^x \rangle = \left(C_0 - C_1 e^{1/k_d} \right) + C_1 e^{-(k-1)/k_d}. \qquad (2)$$

Equation (2) contains three positive constants: C_0 is the variance of the velocity, C_1 is the co-variance between subsequent velocities, and k_d the decay constant that quantifies the extend of the negative correlations.

Please note that C_1 must obey $C_1 \leq \left(1 - e^{-1/k_d} \right) \cdot C_0 / 2$. Similar correlations were seen for v_y and cross-correlations appeared to be negligible.

For the processes specified by Eq. (2), the full mean-square displacement can be calculated analytically [45] and is given by

$$\langle \Delta x_k^2 \rangle = \Delta t^2 \left[k \left(C_0 + \frac{2C_1}{e_1} \right) - \frac{2C_1}{e_1^2} \left(1 - e^{-k/k_d} \right) \right] \qquad (3)$$

with $e_1 = \left(1 - e^{-1/k_d} \right)$. For an extended velocity correlation ($k_d \gg 1$), the MSD grows linearly with time $\left(\Delta x_k^2 \propto k \right)$ both at small times ($k \ll k_d$) and asymptotically also at large times ($k \gg k_d$). In between these limits, there exists a cross-over time-scale that is characterized by a sub-diffusive behavior. In [36] we have shown that for finite negative correlations ($C_1 < 0$), the region of subdiffusion is not entirely determined by the correlation time of the increments $k_d \Delta t$, but also by the strength of the negative correlations which is set by $2C_1/\left(e_1 C_0 \right)$.

The local mean squared displacement (l-MSD) algorithm for this model then yields distributions of the exponent α and the generalized diffusion coefficient D that are close to the values obtained from experimental data. This holds true not only for tracer particle diffusion in the wild-type cells but also if cytoskeleton constituents such as MTs or actin or both are removed by drug treatment [36]. In particular with the removal of both MTs and F-actin, the subdiffusive behavior changes drastically and resembles normal diffusion on intermediate time scales ($\sim 2\,\mathrm{s}$) with a low diffusion coefficient comparable to that observed in glycerol. At very short time scales, the motion is still subdiffusive which could possibly be due to intracellular crowding.

The correlated Gaussian velocity fluctuations used in [36] to describe the intracellular motion can be referred to as a "data-driven" model, because here the origin of the velocity correlations are taken as important model parameters from experiments. However, the agreement between experimental data and the simple model indicates that a non-Gaussianity of the velocity fluctuations does not seem to be responsible for the statistical distributions of subdiffusion quantifiers. Moreover, the approach simplifies the theoretical problem because it demonstrates that one has to look for mechanisms that give rise to extended negative velocity correlations in order to explain subdiffusion of intracellular motion on short time scales.

When using the local MSD algorithm, the parameters for the algorithm, such as window size or the number of MSD points, are crucial and need to be adapted to the specific experiment type, reflecting its biological features.

In Ref. [45] the dependence of the distribution measures were studied for the simple model of velocity correlations given in Eq. (2), which included the equilibrium case of overdamped Brownian motion for $C_1 = 0$, implying uncorrelated increments. An interesting technical question is whether there is an optimal number of MSD points with respect to the reliability of the estimated motion measures. The exponent α, for instance, is obtained for a time window T as the slope of the double-logarithmically plotted MSD. We could use a small number of MSD points (corresponding to short sub-windows) with good statistics (there are many short sub-windows). We could, however, also include more MSD points (corresponding to larger sub-windows) to apparently improve our estimate – these additional points, however, are more noisy (there are fewer large sub-windows within T).

In [45] it was numerically shown that few MSD points are generally the better choice with respect to the reliability of the estimate. For overdamped Brownian motion, just two or three MSD points yield the narrowest distribution of the exponent α. For two MSD points and a sufficiently large time window (20–100 points), the statistical (joint and marginal) distributions of α and $\ln(D)$ can be well approximated by Gaussian functions. In particular, this implies that D obeys a log-normal distribution, which approximates well the distribution of D obtained from experimental data. For

a correlation function of the form given in Eq. (2), explicit expressions can be derived for the variances and covariances characterizing the Gaussian distributions. In fact, for comparable time window and MSD points, simple Brownian motion yields distributions of similar width although with different mean values compared to intracellular motion.

Effect of dimensionality

In [31] we performed 3D tracking of fluorescently labeled DNA polyplexes with a hydrodynamic radius of 200 nm (diameter $\sim$400 nm) within *D. discoideum* cells exhibiting GFP labeled α-tubulin.

Here, the local MSD analysis was performed in 3D and compared to the 2D projection of the 3D path. It was shown that about one third of the active transport phases are incorrectly assigned to diffusive motion upon a 2D projection of the 3D data. In contrast, in analog experiments with human HuH-7 cells the identification of the active phases was barely affected when projecting the data to a 2D plane. This can be explained by the more flattened shape of the HuH-7 cells, where active transport is already tied to the quasi-2D cytoskeleton structure. The 3D particle tracking in *D. discoideum* yields a smooth log-normal distribution of the absolute active transport velocities, exhibiting a peak value of $\hat{v}_{\mathrm{act}} = 0.58\,\mu\mathrm{m\,s}^{-1}$ and an average of $\langle v_{\mathrm{act}} \rangle = 0.69\,\mu\mathrm{m\,s}^{-1}$ [31].

The obtained absolute velocities of the active transport phases are comparable to velocity values of other tracer species of larger diameters [22,23]. These findings elucidate that specific particle properties, like shape and chemical surface properties, are influencing motor-driven active transport in living cells.

Upon 2D projection, the active velocities in *D. discoideum* cells decrease to approximately two third of the 3D values, showing isotropic behavior. In contrast, passive diffusion is found to be anisotropic yielding a deviation by a factor of 0.67 for the 3D diffusion coefficient compared to that of the 2D projection, whereas Brownian diffusion should remain unchanged [31]. The effect of dimensionality on the diffusion coefficient is found to be even stronger for HUH-7 cells, which may be explained by a different cytoskeleton structure, causing a higher degree of deviation (0.31) from normal diffusion, e.g. due to the presence of intermediate filaments [34].

Besides this, intracellular transport phenomena were also examined in 1D by studying trajectories of very small fluorescent quantum dots (QD) of 20 nm diameter within straight axons of pheochromocytoma cells (PC12) [47]. Here, we found events of fast directed transport along MTs with velocities of $v_{\mathrm{act}} = 2\text{–}7\,\mu\mathrm{m\,s}^{-1}$, while QD motion was predominantly subdiffusive with a median diffusion constant of $D^{\mathrm{med}} = 0.41\,\mu\mathrm{m}^2\,\mathrm{s}^{-1}$ in the narrow axon geometry [47].

The work described above shows a complex picture of intracellular dynamics, justifying further detailed studies for the identification of specific transport mechanisms upon interaction with cytoskeleton constituents, acquired with specific imaging techniques. In this view, we report on quantitative investigations of particle transport within wild-type cells of *D. discoideum*, performed by spinning disk confocal microscopy (SDCM) at very fast frame rates of 100 fps and with very high spatial resolution. Imaging is restricted to one fixed focal plane only. In particular, we use highly uniform small fluorescently labeled silica particles with a diameter of 200 nm. For microscopic tracking experiments, the particles are introduced into wild type cells of *D. discoideum* by endocytosis, allowing for motor driven active transport. Particle motion is analyzed in terms of active and passive motility states using the l-MSD algorithm. This way, we obtain the statistical distributions of state parameters [22,23,31,36] and can dissect passive motional phases into phases of subdiffusion, normal diffusion and superdiffusion.

2 Methods

Cell culture:

The axenic *D. discoideum* strains AX2 wild type and LimEΔcc-GFP expressed in LimEΔcc-null (obtained from Dr. Günther Gerisch, MPI for Biochemistry, Martinsried, Germany), were cultivated below a confluency of 40% in HL5 medium (ForMediumTM, Norfolk, United Kingdom) adjusted to $pH = 6.7$, for Lim-GFP in Lim-null complemented by antibiotic Gentamycin (G-418, Biochrom AG, Berlin, Germany) and Blasticidin (Blasticidin S hydrochloride, Sigma Aldrich Chemie GmbH, Taufkirchen, Germany) at a concentration of $10\,\mu\mathrm{g\,mL}^{-1}$, respectively. Measurements have been performed with WT cells, LimEΔcc-GFP expressed in LimEΔcc-null cells have been imaged for Fig. 1a. For microscopy experiments, HL5 medium was substituted by phosphate buffered saline, adjusted at $pH = 6.0$. The cell-PBS-suspension with a cell density of $2 \times 10^7\,\mathrm{cm}^{-3}$ was incubated for 20 min with a concentration of $2 \times 10^{-6}\,\mathrm{g\,cm}^{-3}$ silica particles. Subsequently, the excess particles were removed by centrifugation of the suspension at 1000 rpm for 4 min (Eppendorf MiniSpin® Plus, Eppendorf AG, Hamburg) and the cells were redispersed in 1 ml PBS. The cell-PBS suspension was filled into the observation chamber (composed of a cover glass and custom-made Teflon® frame) and rested for 20 min, allowing the cells to settle down. Experiments have been performed in less than 2h, before onset of starvation, to ensure cell viability.

Silica beads:

Custom-made 200 nm diameter fluorescent silica beads where fabricated according to Larson et al. [48] by an adapted Stöber synthesis. A precursor solution consisting of ethanol (0.17 ml, VWR International GmbH), (3-aminopropyl)triethoxysilane (186.5 mmol, Sigma Aldrich) and tetramethylrhodamine isothiocyanate $(9.3\,\mu\mathrm{mol}$, Sigma Aldrich) was stirred overnight. Subsequently, ethanol (74.3 ml), ammonium hydroxide (6.9 mmol, 30%, Rotipuran®) and water (0.5 mol) were added and stirred for 30 min. After that, ethanol (6.0 ml) and tetraethoxysilane (6.7 mmol, Merck Millipore) were added drop wise over 7 hours. The suspension was continuously stirred for 24 hours and the newly formed silica particles were washed and dispersed in ethanol for further use.

Characterization by scanning electron microscopy showed uniform spherical silica beads with a diameter of $195 \pm 15\,\mathrm{nm}$. The particles where dispersed in PBS by 10 min sonification before adding particles to the cell suspension.

Microscopy:

Fluorescence live cell imaging was performed by spinning disc confocal microscopy. The microscope consists of an inverted microscope (Ti-E, Nikon, Japan), a spinning disk unit (UltraVIEW™ VoX, PerkinElmer®, USA), a CCD camera (C9100-50 Hamamatsu, Germany) and lasers (488 nm and 561 nm, Yokogawa Electric Corporation, Japan). The imaging was performed in a fixed z-plane with a 100× immersion oil objective with a NA of 1.45 at a frame rate of 100 fps, achieving a spatial resolution of ∼600 nm in z-direction and of ∼200 nm in x,y-directions. The tracking algorithm yields center of mass accuracy in the imaging plane of ∼20 nm.

Data analysis:

Particle trajectory analysis was performed using an established tracking routine [49]. Previously, we described a local mean squared displacement (l-MSD) analysis algorithm able to reliably distinguish periods of active and passive motion from 2D trajectories of particles in living cells [23]. This approach is based on the analysis of the local MSD and the directional persistence of the average angle between steps. In short, a l-MSD is calculated for every time point t_i of the particle path over a rolling window of $M = 28$ frames (corresponding to a duration $T = 280\,\text{ms}$) as a function of different lag times τ according to [36]:

$$\langle\Delta R^2\left(\tau\right)\rangle = \langle\left(\mathbf{R}\left(t_i + \tau\right) - \mathbf{R}\left(t_i\right)\right)^2\rangle_{t-T/2 < t_i < t+T/2}. \tag{4}$$

The directional persistence of the bead motion $\Delta\varphi_i\left(\tau\right)$ is measured by the standard deviation of the angle correlation function within the rolling window [23].

The obtained $\langle\Delta R^2\left(\tau\right)\rangle$ is fitted by a power law of the form

$$\frac{\langle\Delta R^2(\tau)\rangle}{l^2} = A \times \left(\frac{\tau}{\tau_0}\right)^\alpha \tag{5}$$

where $l = 1\,\mu\text{m}$ is a chosen unit reference length and $\tau_0 = 1\,\text{s}$ is a reference time, so the prefactor A carries no physical dimension [45].

The value of the α exponent together with the trajectory's angle deviation are used to classify a local trajectory into four motional types

(i) active motion when $[\alpha = 2 \pm \sigma_\alpha]$ and $[\Delta\varphi = \pm\sigma_\varphi]$
(ii) diffusive motion when $[\alpha = 1 \pm \sigma_\alpha]$,
(iii) subdiffusive motion when $[0 \leq \alpha \leq 0.7]$,
(iv) and superdiffusive motion when state is not active and $[1.3 \leq \alpha \leq 1.7]$

with $\sigma_\alpha = 0.3$ and $\sigma_\varphi = 0.9\,\text{rad}$. For diffusive motion, a generalized diffusion coefficient D can be retrieved from the prefactor A of the power-law fit of Eq. (5) by

$$D = \frac{\langle\Delta R^2(\tau_0)\rangle}{2d\tau_0} = \frac{Al^2}{2d\tau_0} \tag{6}$$

where d is the number of spatial dimensions [45]. This way, diffusion coefficients D_{sub}, D_{diff} and D_{super} are calculated for subdiffusive, normal diffusive and superdiffusive states, respectively. Note that for anomalous diffusion, the value in Eq. (6) will strongly depend on the window size. For active states a new fit of the data is performed with $\alpha = 2$, returning the local absolute velocity v_{act} by

$$\langle\Delta R^2(\tau)\rangle = v_{\text{act}}^2 \cdot \tau^2. \tag{7}$$

The distributions of the particle motion parameters obtained by the l-MSD analysis are fitted with empirically chosen functions. The absolute velocities of all events and of the diffusive states are fitted with generalized log-logistic functions of type Burr XII [50]. The distributions of the active motion state velocities and of the diffusion coefficients are fitted with log-normal distribution functions.
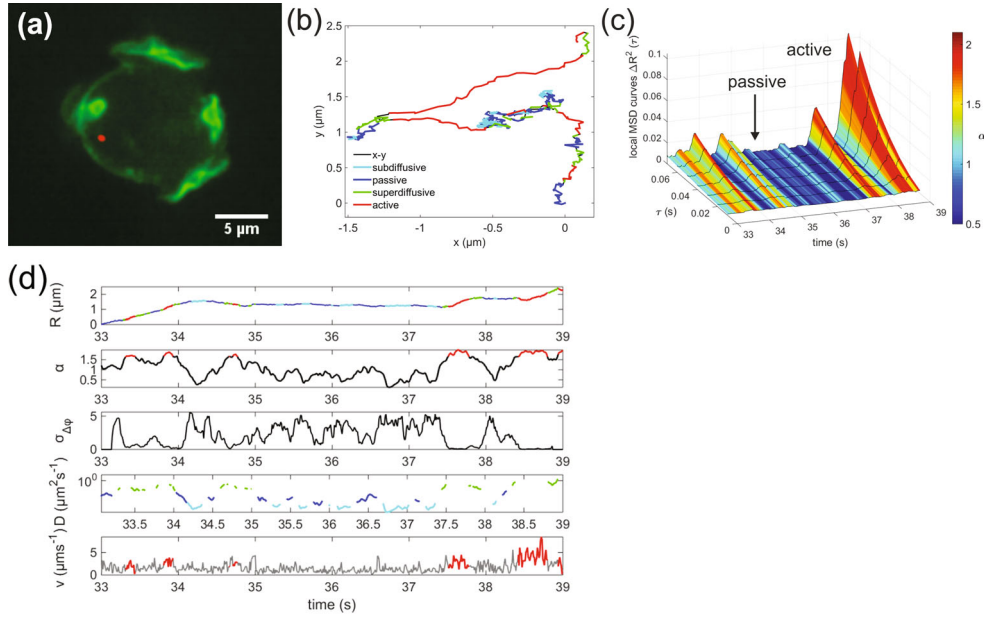
Fig. 1. Bead trajectory analysis in living *D. discoideum cell*. (a) SDCM fluorescence image of a 200 nm silica particle (red) within a living *D. discoideum* cell with GFP labeled lim proteins (green). (b) Color-coded 2D track of the silica particle highlighting motion phases of active transport (red), sub- (cyan), normal (blue), and super-diffusive (green) motion as derived from the l-MSD analysis. (c) Local MSD of the silica particle as a function of lag time τ over experiment time, with corresponding l-MSD exponent α illustrated by color-code. (d) Time courses of particle motion parameters, from top to bottom: silica particle position R, l-MSD exponent α, angle deviation $\sigma_{\Delta\varphi}$, diffusion coefficient D retrieved during the passive diffusive states, instantaneous particle velocity v_{inst} (light gray) and algorithm-retrieved velocity v_{act} during the active transport states (red).

3 Results and discussion

In this work, we study the intracellular transport of endocytosed silica particles of spherical shape and 200 nm diameter. Imaging was performed in a fixed narrow focal plane (2D imaging) by spinning disk confocal microscopy (SDCM), minimizing projections and therefore diminishing misinterpretation of motion states that can reach into the third dimension. Silica particle were tracked in 25 different cells, yielding a total of 132,000 data points.

Figure 1a shows an example of a fluorescence image of a 200 nm particle (red) in a *D. discoideum* cell with GFP labeled lim proteins (green). Four motility states of a particle are distinguished by the l-MSD analysis, as illustrated by the color-coded trajectory in Fig. 1b, showing phases of active transport (red) and diffusive motion, where the latter phase is subdivided into sub- (cyan), normal (blue), and superdiffusive (green) states. In Fig. 1c, local MSDs are displayed as a function of experiment time and different lag times τ, with the corresponding α-exponents illustrated by color code. Further, motion parameter analysis is visualized as a function of experiment time in Fig. 1d, displaying the silica particle position R, the l-MSD exponent α, the standard deviation of the angle deviation $\sigma_{\Delta\varphi}$, the diffusion coefficient D, and the instantaneous velocity v_{inst}.

For quantitative analysis, motion states are evaluated by the statistical distributions of parameters obtained from the l-MSD algorithm. Figure 2 shows the distributions of the exponent α (a), the absolute instantaneous velocity v-distributions of all motion events (b), and the absolute velocity $|v_{\mathrm{act}}|$ during active states (c). The distributions of diffusion coefficients D_{sub}, D_{diff} (suffix "diff" refers here to normal diffusion states) and D_{super} retrieved during the passive motion phases are shown in Fig. 3a. The corresponding average and median values are given in Table 1, together with the peak values of the distributions, which are determined by fitting with empirically chosen functions.

The distribution of the calculated l-MSD exponents α is shown in Fig. 2a, elucidating the partitioning into four motion states assigned to active transport (red), sub- (cyan), normal (blue) and superdiffusion (green). The overall distribution peaks below $\alpha = 1$, with a mean value of $\langle \alpha \rangle = 0.87$ and a median $\alpha^{\mathrm{med}} = 0.83$. We notice that the contribution of active states is quite low compared to results obtained by former studies of endocytosed particles within living cells of *D. discoideum*, where a frequent appearance of exponents $\alpha > 1$ indicated a generally high directed transport activity [22,31]. In the present study, we selectively obtain tracks of particle motion in x,y-dimensions by confocal imaging within a fixed focal plane. Therefore, events of fast, directed active transport are underrepresented in the obtained distribution of motion states, because in most cases tracer particles only cross the narrow focal volume and cannot be tracked for longer times. On the other hand, this selective tracking of planar motion in x,y-planes allows to obtain particle velocities with particularly high precision.

We show the distribution of the obtained absolute particle velocities (grey) in Fig. 2b, together with the distributions of the four investigated motional states. All these distributions are fitted by empirically chosen functions. The distribution of the active velocities is fitted to a log-normal distribution function with a peak value of $\langle v_{\mathrm{act}} \rangle = 2.5\,\mu\mathrm{m\,s}^{-1}$, while the passive phase distributions are corresponding to generalized log-logistic functions of Burr type XII. For the subdiffusive phase we find a peak value of $v_{\mathrm{sub}} = 0.9\,\mu\mathrm{m\,s}^{-1}$, for normal diffusive phases a peak value of $v_{\mathrm{diff}} = 1.2\,\mu\mathrm{m\,s}^{-1}$ and for superdiffusion a peak velocity of $v_{\mathrm{super}} = 1.5\,\mu\mathrm{m\,s}^{-1}$. The overall distribution of the absolute velocities also shows Burr-shape, with a peak value of $v_{\mathrm{inst}} = 1.1\,\mu\mathrm{m\,s}^{-1}$. Comparing the distributions, we notice a trend of increasing particle velocity with increasing α exponents, as expected. The obtained velocity values for particles with 200 nm diameter are significantly higher than absolute velocities found before for latex particles of 520 nm diameter and for Fe_3O_4 beads of $1.42\,\mu\mathrm{m}$ diameter [43], suggesting a size-dependence of active and passive motion speed of particles within living cells.

Active transport states

The distribution of active absolute values of velocities of silica particles with 200 nm diameter moving within *D. discoideum* cells is shown in Fig. 2c, together with the corresponding cumulative distribution. By quantitative analysis, we find a mean value of the absolute velocities during the active states of $\langle v_{\mathrm{act}} \rangle = 2.8\,\mu\mathrm{m\,s}^{-1}$, which is significantly higher than in previous studies [22,23], where active transport of Fe_3O_4 beads with $1.4\,\mu\mathrm{m}$ [23] and with $1.0\,\mu\mathrm{m}$ diameter [22] in *D. discoideum* cells was observed with average absolute values of velocities of $\langle v_{\mathrm{act}} \rangle = 0.39\,\mu\mathrm{m\,s}^{-1}$ [23], and $\langle v_{\mathrm{act}} \rangle = 0.35\,\mu\mathrm{m\,s}^{-1}$ [22], respectively. Earlier investigations with Fe_3O_4 particles of $1.4\,\mu\mathrm{m}$ diameter vs. small latex beads of 520 nm diameter suggested an increase of active absolute velocities with decreasing particle size, from a range of 0.5–$1.5\,\mu\mathrm{m\,s}^{-1}$ up to a range of 1–$3\,\mu\mathrm{m\,s}^{-1}$ [43]. Assuming an increase of absolute active velocities
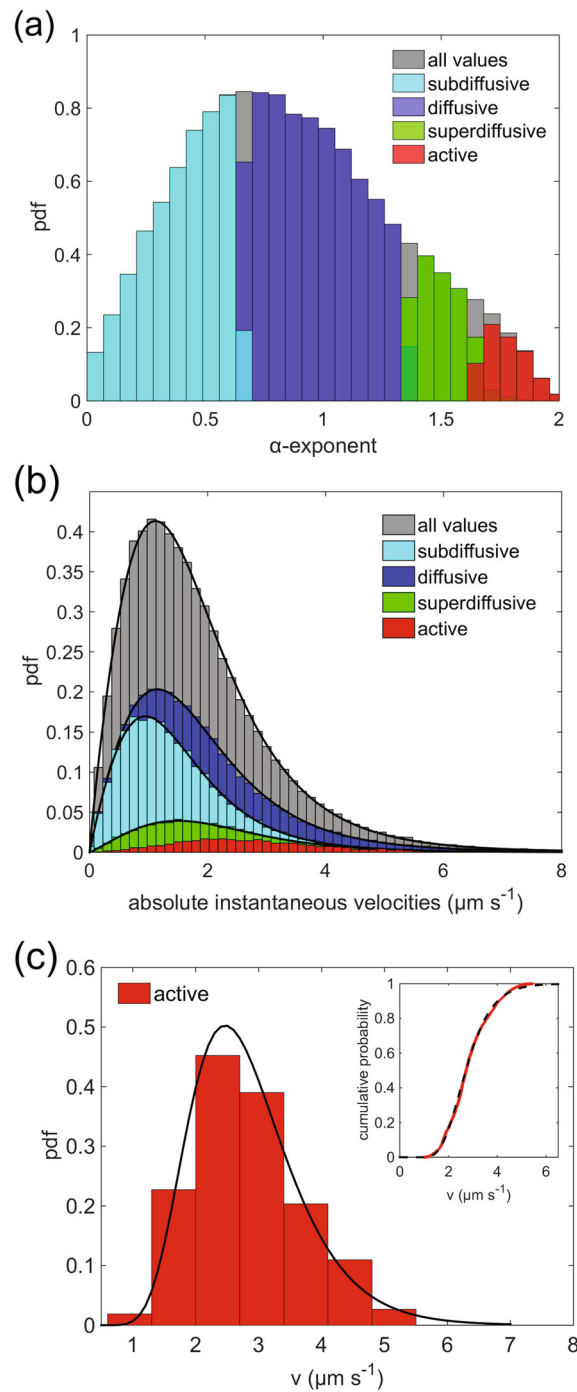
Fig. 2. Analysis of active and passive transport in living cells of *D. discoideum.* (a) Distribution of l-MSD α-exponents, showing different states assigned to active transport (red), sub- (cyan), normal (blue) and superdiffusion (green). (b) Distributions of absolute velocities of all events (gray), and of the different motion states corresponding to Fig. 2(a). Distributions of absolute velocities fitted by Burr-function of type XII. (c) Distribution of active state velocities obtained by the l-MSD algorithm, fitted with a log-normal function. Inset shows corresponding cumulative distribution function with log-normal fit (dashed line).

Table 1. Motion parameters obtained by l-MSD analysis, exponents $\boldsymbol{\alpha}$, instantaneous velocities $\boldsymbol{v}$, diffusion coefficients $\boldsymbol{D}$, and transport velocities during active states of 200 nm silica particles within WT cells of *D. discoideum*.

	Mean	Median	Peak value
α	0.87	0.83	
α_{sub}	0.41	0.43	
α_{diff}	0.96	0.95	
α_{super}	1.50	1.49	
α_{act}	1.8	1.8	
$v_{\text{inst}}\,\left(\mu\text{m s}^{-1}\right)$	1.9	1.6	1.1
$v_{\text{inst,sub}}\,\left(\mu\text{m s}^{-1}\right)$	1.6	1.3	0.9
$v_{\text{inst,diff}}\,\left(\mu\text{m s}^{-1}\right)$	1.9	1.6	1.2
$v_{\text{inst,super}}\,\left(\mu\text{m s}^{-1}\right)$	2.2	2.0	1.5
$D_{\text{all}}\,\left(\mu\text{m}^2\,\text{s}^{-1}\right)$	6.6×10^{-2}	1.0×10^{-2}	1.6×10^{-2}
$D_{\text{sub}}\,\left(\mu\text{m}^2\,\text{s}^{-1}\right)$	4.4×10^{-3}	2.8×10^{-3}	8.7×10^{-3}
$D_{\text{diff}}\,\left(\mu\text{m}^2\,\text{s}^{-1}\right)$	4.9×10^{-2}	3.0×10^{-2}	7.8×10^{-2}
$D_{\text{super}}\,\left(\mu\text{m}^2\,\text{s}^{-1}\right)$	3.0×10^{-1}	2.2×10^{-1}	3.8×10^{-1}
$\langle v_{\text{act}}\rangle\,\left(\mu\text{m s}^{-1}\right)$	2.8	2.7	2.5

with decreasing particle size, the different velocity values found for the silica particles, as compared to larger Fe_3O_4 particles, appear well consistent with former results.

Tracking of DNA polyplexes with a hydrodynamic radius of 200 nm (twice as large in diameter as the silica beads) yielded an average absolute active velocity of active states $\langle v_{act}\rangle = 0.58\,\mu\text{m s}^{-1}$ [31], consistent lower than the present results with silica beads [15]. Probably the different chemical surface entities and the non-spherical shape of the particles led to even bigger vesicle formation around DNA polyplexes, slowing down active transport by the crowded intracellular environment.

Diffusive motion states

We selectively assess subdiffusion, normal diffusion as well as superdiffusion phases and the respective diffusion coefficients. Figure 3a shows distributions of the diffusion coefficients for these three states, fitted by log-normal functions. The inset of Fig. 3a shows the overall distribution of the diffusion coefficients, also fitted by a log-normal function. All distributions of the diffusion coefficients are in good agreement with the log-normal fits [45].

Upon comparison with former results [22,23,36], we notice that the average diffusion coefficient of all diffusive states $\langle D_{\text{all}}\rangle = 6.6 \times 10^{-2}\,\mu\text{m}^2\,\text{s}^{-1}$ obtained for the endocytosed 200 nm silica particles within WT cells is of the same order of magnitude as the diffusion constant $\langle D\rangle = 6.1 \times 10^{-2}\,\mu\text{m}^2\,\text{s}^{-1}$ [36] obtained with polymer-coated particles of 150 nm diameter in WT cells [36]. On the other hand, the overall diffusion constant for the 200 nm particles deviates from passive diffusion coefficients of $\langle D\rangle = 6.1 \times 10^{-3}\,\mu\text{m}^2\,\text{s}^{-1}$ [23] and of $\langle D\rangle = 9.8 \times 10^{-3}\,\mu\text{m}^2\,\text{s}^{-1}$ [22] obtained before with Fe_3O_4 particles of 1.45 μm [23] and of 1.0 μm diameter [22], respectively. This suggests a general dependence of intracellular passive diffusion coefficients on the size of the tracer particles [9,34,51,52]. Also the different materials of the tracer particles may render significant effects on passive intracellular diffusion, as suggested in particular by comparison with a diffusion constant $\langle D\rangle = 8.8 \times 10^{-3}\,\mu\text{m}^2\,\text{s}^{-1}$ obtained before with DNA polyplexes of $\sim$400 nm diameter [31].

By extracting the motion phases for l-MSD α-values of about 1, we selectively assess states of normal diffusion of our 200 nm silica particles. Using the average
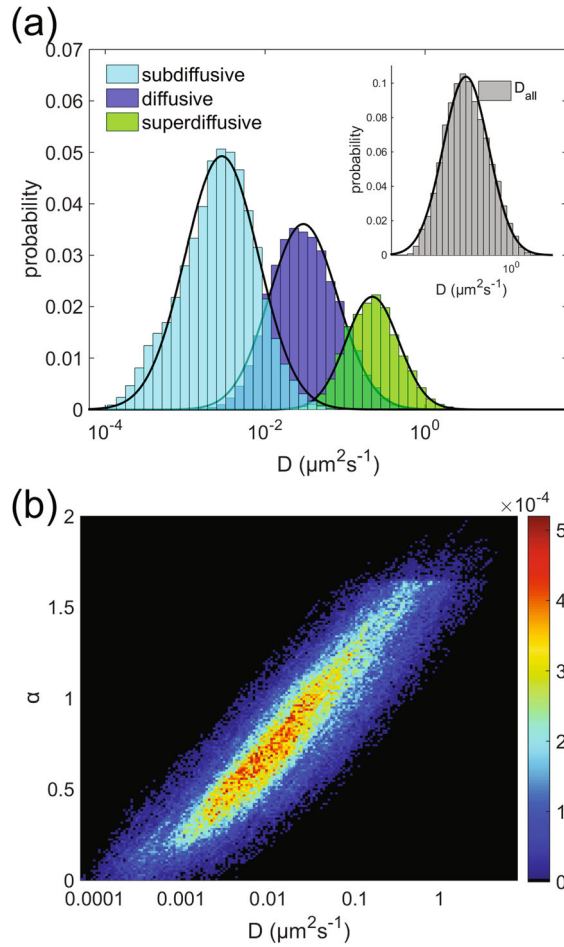
Fig. 3. Distributions of passive transport state paramters: (a) Distributions of coefficients of subdiffusive D_{sub} (cyan), normal diffusive D_{diff} (blue), and superdiffusive D_{super} (green) states. Inset shows overall distribution of all diffusion coefficient values D_{all}. Distributions of the diffusion coefficients are in agreement with log-normal fits [45]. (b) Joint distribution of α- and D-values showing monotonous, yet nonlinear relation.

value $\langle D_{diff} \rangle = 4.9 \times 10^{-2} \, \mu m^2 \, s^{-1}$, we calculate an effective cytoplasm viscosity of $\eta_c = 4.4 \times 10^{-2} \, Pa \, s$ in good agreement with [23].

The sectioning of motional states by α-values, as shown in Fig. 2a, yields the mean values $\langle \alpha_{sub} \rangle = 0.41$ for the subdiffusive and $\langle \alpha_{super} \rangle = 1.50$ for the superdiffusive states. This partitioning yields mean values of the diffusion constants of $\langle D_{sub} \rangle = 4.4 \times 10^{-3} \mu m^2 \, s^{-1}$ and $\langle D_{super} \rangle = 3.3 \times 10^{-1} \mu m^2 \, s^{-1}$, respectively. The spread of the diffusion coefficient over two orders of magnitude can be explained by the inhomogeneous intracellular regimes the bead is exploring. While a very crowded intracellular milieu yields low diffusion coefficients, regions of less crowding and active processes in the cell exhibit higher values of diffusion coefficients. Figure 3b shows the joint distribution of the α- and D-values, revealing a monotonous, yet nonlinear relation in accordance to former results for WT cells [36].

4 Conclusion

We studied intracellular transport of 200 nm silica particles within living cells of *D. discoideum* by spinning disk confocal imaging in one focal plane at a frame rate of 100 fps. Using single particle tracking and local mean squared displacement (l-MSD) analyses, we demonstrate the impact of intracellular architecture and cytoskeleton dynamics on anomalous diffusion and active transport. Significantly, active motor-driven processes can be reliably differentiated from diffusive processes, which are divided into states of sub-, normal, and superdiffusive motion. Furthermore, important parameters like particle velocity and the local diffusion coefficient are determined. In particular, the average active transport velocity found to be $\langle v_{\mathrm{act}} \rangle = 2.8\,\mu\mathrm{m\,s^{-1}}$, derived by a high accuracy imaging method. Moreover, we show that the diffusion constants of 200 nm silica particles in *D. discoideum* wild type cells span more than two orders of magnitude, reflecting the spread in local micro-environments of the cell interior.

By our results, we highlight the potential of the l-MSD analysis for unravelling intracellular dynamics with high-resolution microscopy imaging. This approach can also be used for detailed investigations of cellular motion behavior [53,54]. These investigations will prove of ample importance for medical applications like targeted treatment by nano-sized drug carriers or innovative diagnostic-assays.

References

1. T. Pederson, Nat. Cell Biol. **2** (2000)
2. M. Guthold, X. Zhu, C. Rivetti, G. Yang, N.H. Thomson, S. Kasas, H.G. Hansma, B. Smith, P.K. Hansma, C. Bustamante, Biophys. J. **77**, 4 (1999)
3. H. Berry, Biophys. J. **83**, 4 (2002)
4. J. Valdez-Taubas, H.R. Pelham, Curr. Biol. **13**, 18 (2003)
5. M. Weiss, M. Elsner, F. Kartberg, T. Nilsson, Biophys. J. **87**, 5 (2004)
6. F. Höfling, T. Franosch, Rep. Prog. Phys. **76**, 4 (2013)
7. F.C. MacKintosh, C.F. Schmidt, Curr. Opin. Cell Biol. **22**, 1 (2010)
8. I.M. Sokolov, Soft Matter **8**, 35 (2012)
9. D. Stauffer, C. Schulze, D.W. Heermann, J. Biol. Phys. **33**, 4 (2007)
10. M.V. Chubynsky, G.W. Slater, Phys. Rev. Lett. **113**, 9 (2014)
11. Z. Schuss, A. Singer, D. Holcman, PNAS **104**, 41 (2007)
12. D.S. Grebenkov, M. Vahabi, E. Bertseva, L. Forró, S. Jeney, Phys. Rev. E **88**, 4 (2013)
13. P. Romanczuk, M. Bär, W. Ebeling, B. Lindner, L. Schimansky-Geier, Eur. Phys. J. Special Topics **202**, 1 (2012)
14. C.P. Brangwynne, G.H. Koenderink, F.C. MacKintosh, D.A. Weitz, Trends Cell Biol. **19**, 9 (2009)
15. I. Goychuk, V.O. Kharchenko, R. Metzler, PLoS ONE **9**, 3 (2014)
16. G. Guigas, M. Weiss, Biophys. J. **94**, 1 (2008)
17. C. Kural, Science **308**, 5727 (2005)
18. S. Rice, A.W. Lin, D. Safer, C.L. Hart, N. Naber, B.O. Carragher, S.M. Cain, E. Pechatnikova, E.M. Wilson-Kubalek, M. Whittaker, E. Pate, R. Cooke, E.W. Taylor, R.A. Milligan, R.D. Vale, Nature **402**, 6763 (1999)
19. A. Kahana, G. Kenan, M. Feingold, M. Elbaum, R. Granek, Phys. Rev. E **78**, 5 (2008)
20. E. Sackmann, F. Keber, D. Heinrich, Annu. Rev. Condens. Matter Phys. **1**, 1 (2010)
21. C. Loverdo, O. Bénichou, M. Moreau, R. Voituriez, Nat. Phys. **4**, 2 (2008)
22. J. Mahowald, D. Arcizet, D. Heinrich, Chem. Phys. Chem. **10**, 9 (2009)
23. D. Arcizet, B. Meier, E. Sackmann, J. Rädler, D. Heinrich, Phys. Rev. Lett. **101**, 24 (2008)
24. N. Leijnse, J.-H. Jeon, S. Loft, R. Metzler, L.B. Oddershede, Eur. Phys. J. Special Topics **204**, 1 (2012)
25. D. Weihs, T.G. Mason, M.A. Teitell, Biophys. J. **91**, 11 (2006)

26. S. Courty, C. Luccardini, Y. Bellaiche, G. Cappello, M. Dahan, Nano Lett. **6**, 7 (2006)
27. J. Gelles, B.J. Schnapp, M.P. Sheetz, Nature **331**, 6155 (1988)
28. G.M. Lee, A. Ishihara, K.A. Jacobson, PNAS **88** (1991)
29. I. Golding, E. Cox, Phys. Rev. Lett. **96**, 9 (2006)
30. R. Metzler, J. Klafter, Phys. Rep. **339**, 1 (2000)
31. A. Dupont, M. Gorelashvili, V. Schüller, F. Wehnekamp, D. Arcizet, Y. Katayama, D.C. Lamb, D. Heinrich, New J. Phys. **15**, 7 (2013)
32. J.-H. Jeon, A.V. Chechkin, R. Metzler, Physical Chem. Chem. Phys. **16**, 30 (2014)
33. M.J. Saxton, K. Jacobson, Annu. Rev. Biophys. Biomol. Struct. **26** (1997)
34. A. Caspi, R. Granek, M. Elbaum, Phys. Rev. E **66**, 1 (2002)
35. F. Bartumeus, J. Catalan, U. Fulco, M. Lyra, G. Viswanathan, Phys. Rev. Lett. **88**, 9 (2002)
36. M. Otten, A. Nandi, D. Arcizet, M. Gorelashvili, B. Lindner, D. Heinrich, Biophys. J. **102**, 4 (2012)
37. S. Ma, P. Fey, R.L. Chisholm, Biochim. Biophys. Acta **1525**, 3 (2001)
38. G. Gerisch, A. Muller-Taubenberger, Methods Enzymol **361** (2003)
39. D. Heinrich, E. Sackmann, Acta Biomater. **2**, 6 (2006)
40. M.J. Müller, S. Klump, R. Lipowsky, PNAS **12**, 105 (2008)
41. M.A. Welte, Curr. Biol. **14**, 13 (2004)
42. C.B. Korn, S. Klumpp, R. Lipowsky, U.S. Schwarz, J. Chem. Phys. **131**, 24 (2009)
43. W. Feneberg, M. Westphal, E. Sackmann, Eur. Biophys. J. **30**, 4 (2001)
44. S. Marion, J. Cell Sci. **117**, 15 (2004)
45. A. Nandi, D. Heinrich, B. Lindner, Phys. Rev. E **86**, 2 (2012)
46. Box, George E.P, G.M. Jenkins, G.C. Reinsel, *Time series analysis. Forecasting and control* (John Wiley, Hoboken, N.J., 2008)
47. C. Pelzl, D. Arcizet, G. Piontek, J. Schlegel, D. Heinrich, Chem. Phys. Chem. **10**, 16 (2009)
48. D.R. Larson, H. Ow, H.D. Vishwasrao, A.A. Heikal, U. Wiesner, W.W. Webb, Chem. Mater. **20**, 8 (2008)
49. M.B. Smith, E. Karatekin, A. Gohlke, H. Mizuno, N. Watanabe, D. Vavylonis, Biophys. J. **101**, 7 (2011)
50. I.W. Burr, Ann. Math. Statist. **13**, 2 (1942)
51. L. Hou, F. Lanni, K. Luby-Phelps, Biophys. J. **58**, 1 (1990)
52. I.L. Novak, P. Kraikivski, B.M. Slepchenko, Biophys. J. **97**, 3 (2009)
53. D. Arcizet, S. Capito, M. Gorelashvili, C. Leonhardt, M. Vollmer, S. Youssef, S. Rappl, D. Heinrich, Soft Matter **8**, 5 (2012)
54. M. Gorelashvili, M. Emmert, K.F. Hodeck, D. Heinrich, New J. Phys. **16**, 7 (2014)